Journal of Materials Chemistry A

ROYAL SOCIETY OF CHEMISTRY

PAPER

View Article Online
View Journal

Cite this: DOI: 10.1039/d2ta04840j

Impact of non-stoichiometry on ion migration and photovoltaic performance of formamidinium-based perovskite solar cells†

Stijn Lammar, ‡[abcd] Renán Escalante, ‡[e] Antonio J. Riquelme, [e] Sandra Jenatsch, [f] Beat Ruhstaller, *[f] Gerko Oskam, [eg] Tom Aernouts*[bcd] and Juan A. Anta *[e]

Ion migration mechanisms are often behind degradation pathways in perovskite solar cells under operating conditions. In this work we look at the effect of non-stoichiometric compositions in mixed caesium/formamidinium inverted perovskite solar cells (PSC) on their performance and short-term degradation. From impedance measurements and drift-diffusion modelling we infer that the excess of the formamidinium precursor (FAI) in the perovskite active layer leads to an acceleration of the ion dynamics due to the creation of mobile crystalline defects. In contrast to what could be expected, this feature is not correlated with faster degradation. Instead, more stable devices are demonstrated when a non-stoichiometric composition is used. Addition of excess FAI also modifies the recombination kinetics: a non-monotonous variation of the open-circuit photovoltage and the recombination rate is observed, with optimal performance found for a composition of 1.0–1.5% excess of FAI.

Received 19th June 2022
Accepted 5th August 2022

DOI: 10.1039/d2ta04840j

rsc.li/materials-a

1. Introduction

Lead halide perovskites are solid semiconductors with mixed ionic-electronic charge conduction features.[1,2] When pure, they can be described by the general chemical formula $APbX_3$, where A is a inorganic or organic cation, and X is a halide anion. Perovskites are, in essence, ionic compounds with peculiar properties under optical excitation that leads to exceptional optoelectronic performance. In particular for solar cell applications perovskite solar cells (PSCs) have increased their efficiency enormously in a time span of less than 10 years, with record values above 25% for single devices already reported, as well as nearly 30% for tandem devices.[3]

In spite of this relatively quick success, which has attracted the interest of many research teams and funding agencies all over the globe, the ionic character and hybrid composition of perovskites leads to complications in terms of proper photovoltaic characterization,[4] lack of reproducibility and consistency of data among different laboratories[5] and, most importantly, lack of stability in the medium and long term.[6–9] One good example of that is the well-known light-induced phase segregation of mixed iodide/bromide perovskites.[10,11]

Many efforts to improve the stability (as well as the efficiency) of PSCs have involved the partial substitution of the A cation. For instance, inclusion of relatively small amounts of caesium ions into the crystalline structure have demonstrated to result in more robust devices.[12] On the other hand, promising results have been obtained with formamidinium-based PSCs ($FAPbI_3$).[13,14] However, the structural phase that allows for the absorption of photons and the creation of electron–hole pairs, the α-black phase, is unstable, and rapidly decays to the δ-yellow phase, useless for solar cell applications.[15] Stabilization of the formamidinium black phase has been accomplished, among several other strategies, by addition of small amounts of caesium (together with mixing iodide and bromide)[16] or quantum dots.[17,18] In all these reports the stabilization of the material appears to be linked to the creation of defects in the crystalline structure.

Photovoltaic performance in PSC is also strongly dependent on recombination kinetics. Charge collection efficiencies are determined by the interplay between recombination in the bulk and at the interfaces[19–22] and the internal electric field created by ion migration and ion accumulation at the interfaces.[23–26] Thus, electronic recombination and ion motion phenomena are

[a]Department of Electrical Engineering (ESAT), Katholieke Universiteit Leuven, Kasteelpark Arenberg 10, 3001 Leuven, Belgium
[b]Imec, imo-imomec, Thin Film PV Technology – partner in Solliance, Thor Park 8320, 3600 Genk, Belgium. E-mail: anta@upo.es
[c]EnergyVille, imo-imomec, Thor Park 8320, 3600 Genk, Belgium
[d]Hasselt University, imo-imomec, Martelarenlaan 42, 3500 Hasselt, Belgium
[e]Department of Physical, Chemical and Natural Systems, Universidad Pablo de Olavide, Carretera de Utrera km 1, Sevilla 41013, Spain
[f]Fluxim AG, Loft 313, Katharina-Sulzer-Platz 2, 8400 Winterthur, Switzerland
[g]Department of Applied Physics, CINVESTAV-IPN, Antigua Carretera a Progreso km 6, Mérida, Yucatán 97310, Mexico

† Electronic supplementary information (ESI) available. See https://doi.org/10.1039/d2ta04840j

‡ Both authors have equal contributions.

linked to each other in PSC under operation. This connection explains the well-known hysteresis features[27,28] and the correlation between low and high frequency signals in impedance spectroscopy and other small-perturbation measurements.[20,23,26,29] Extraction of ionic features in perovskites from electrical measurements is not easy and several attempts involving impedance,[26,30–32] intensity-modulated photocurrent spectroscopy,[2,33] temperature-dependent transient capacitance measurements,[34,35] open-circuit voltage decays[36] and photoluminescence[37] can be found in the specialized literature.

In this work we explore the effect of non-stoichiometry on the performance and stability of mixed caesium/formamidinium inverted PSCs. In previous work by some of the authors[38] it was found that stoichiometry is a very important parameter for improved photostability under light soaking at the maximum power point. By optimizing the annealing time during perovskite deposition with FACl as an additive it was possible to control the surface and bulk stoichiometry by creating Pb-rich surfaces. These modified, non-stoichiometric films were found to be much more photostable, and these results prompted us to embark on a more fundamental investigation. That an excess of FA precursor could be beneficial for performance and stability has also been reported by Boyd *et al.*[39] and Deng *et al.*[40] The former found that detrimental redox reactions at the metal oxide/perovskite interface can be avoided by a adding a small excess of A-cation precursor. Interestingly, the improvement in the open-circuit photovoltage of the device was linked to a reduction of the hole extraction barrier and a minimization of surface recombination. On the other hand, Deng *et al.* showed the importance of the creation and "compensation" of ionic defects when the stoichiometry of the perovskite film is altered, and how this can lead to better photostability.

In this work we start from the idea that by adding small amounts of formamidinium iodide (FAI) in excess during perovskite synthesis we are enforcing the formation of crystalline defects in the active layer. The addition of excess FAI modifies the recombination kinetics in a non-monotonous way but, in addition, also leads to improved device stability under illumination. Interestingly, we observe that this behaviour coincides with enhanced ionic migration (as detected in the low frequency regime of impedance measurements) and inverted hysteresis features at low scan rates. We use drift-diffusion modelling to confirm this interpretation and to infer values of the ion mobility and the ion concentration that explain the experimental results.

2. Experimental and modelling details

Details of the fabrication of the perovskite solar cells devices with composition $Cs_{0.10}FA_{0.90}PbI_{2.855}Br_{0.145}$ plus an "x" molar excess of FA or Cs with respect to the Pb concentration can be found in the ESI.† *JV* measurements were performed in a nitrogen filled glovebox using a Keithley 2602A source-measure unit and a Abet solar simulator with simulated 100 mW cm^{-2} AM1.5G illumination from a 450 W xenon lamp (Abet Sun 2000). A fan was implemented to keep the PSC temperature at 30 °C. The illumination intensity was calibrated with a Fraunhofer ISE's WPVS reference solar cell (Type: RS-ID-4). The solar cells were measured between −0.2 V and 1.2 V with a voltage step of 0.01 V and delay time of either 0.01 s or 0.1 s, corresponding to a measurement rate of ∼0.8 and ∼0.1 V s^{-1}, respectively. The MPPT was conducted in the Abet solar simulator mentioned above. We followed the "Tracking algorithm" from our previous work by Rakocevic *et al.*[41]

JV curves under red light illumination (LED) were measured at different scan rates between 1 V s^{-1} and 1 mV s^{-1} to study the hysteresis of the cells. The hysteresis measurement consists of a *JV* curve measured at nine scan rates: 1000, 800, 600, 400, 200, 100, 50, 10 and 1 mV s^{-1}. The measurement starts at voltage positive of the V_{OC}, goes to short-circuit and slightly negative voltages, and back to V_{OC} and more positive voltage: 1.2 V to −0.1 V (reverse), followed by −0.1 V to 1.2 V (forward). The reverse and forward measurements were compared by determining the area under the curve to calculate the degree of hysteresis (DoH, see below). Results are collected in Table S1.†

The impedance spectroscopy (IS) studies were conducted with a red and blue LEDs. We also carried out temperature-controlled impedance experiments with red illumination. The red LED illumination was set using the reference cell (0.0% FAI-excess) approaching the V_{OC} obtained at 1-sun illumination. The IS was performed at five light intensities at V_{OC}, with a known small perturbation with frequencies from 10^6 to 10^{-2} Hz. The IS at different temperatures was done from 10 to 35 °C using the red LED. In addition, before and after each IS measurement a *JV* curve was measured to rule out significant degradation.

Numerical drift-diffusion simulations were carried out using the simulations software SETFOS 5.3 from Fluxim.[42] Details of the simulations and a table of the parameters used to model the experimental devices are presented in the ESI.†

3. Results

Photovoltaic performance and stability data for the studied PSCs under 1-sun solar illumination are presented in Fig. 1.

Reference devices (with no FAI excess) show excellence performance with photoconversion efficiencies (PCE) between 16 and 19% (Fig. S1†). Addition of excess FAI first increases the V_{OC} and the PCE but if the amount of added FAI is too large, a deleterious effect on performance is observed, in particular at short-circuit. In summary, an optimum non-stoichiometric composition with a FAI excess between 1 and 1.5% maximizes both the V_{OC} and the overall performance of the solar cell. It is worth noting that small differences in the photovoltaic parameters are observed between different batches of samples (see for instance Fig. S6†). However, the overall trends are the same, and the differences are always kept within the experimental uncertainty of 1–2% in PCE values as shown in Fig. S1.†

The use of non-stoichiometric compositions also has a strong impact on the stability of the device under illumination (Fig. 1b). For low values of FAI excess the efficiency deteriorates steadily in the first 10–20 minutes of light soaking. In contrast, for higher values of FAI excess, the performance is low at the

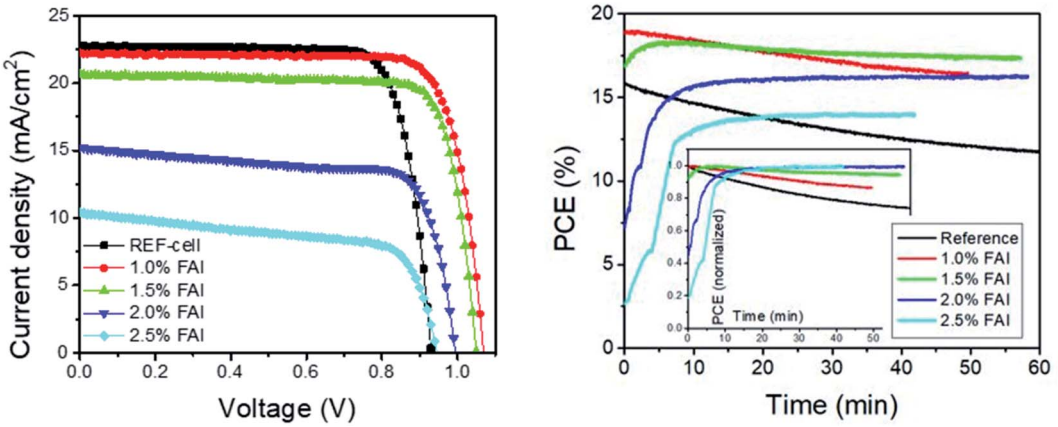

Fig. 1 (a) *JV* characteristics of the studied cells under AM1.5G 1-sun illumination. The scan rate was 100 mV s^{-1}. (b) Photoconversion efficiency (PCE) at the maximum power point under 1-sun illumination as a function of time.

beginning but rapidly increases and then stabilizes. This behaviour is mainly due to the time variation of the photocurrent in the maximum power point (see Fig. S2†). The larger the FAI content, the lower the initial value of the photocurrent, and the more pronounced the stabilization effect at longer times. It is worth noticing that even for stoichiometric devices and with low FAI excess, the degradation process is reversible and the initial values of the performance can be recovered once light soaking is stopped. We also observed a longer rise time before reaching the photostationary state for cells with higher FAI excess. Both observations point to the presence of a second migrating ionic defect generated during FAI doping and with a much slower mobility. Indications of slow phase segregation processes upon illumination and subsequent dark recovery have previously been reported.[43,44]

Interestingly, very similar trends are observed when the departure from the stoichiometry composition is caused by addition of small amounts of CsI instead (see Fig. S3†). It must be highlighted that materials characterization of the non-stoichiometric samples does not reveal any significant alteration in their crystalline structures or film morphologies with respect to the reference (see Fig. S4† for XRD patterns and SEM images). Addition of excess FAI does not modify the band gap either, as inferred from the photoluminescence spectrum (Fig. S5†).

We have extracted the hysteresis index of the devices for the studied compositions. Results as a function of the scan rate are presented in the ESI (Fig. S6†). The hysteresis index or degree of hysteresis (DoH) is defined *via*[24]

$$\mathrm{DoH} = 100\frac{A_{\mathrm{rev}} - A_{\mathrm{for}}}{\max.\left(A_{\mathrm{rev}},\ A_{\mathrm{for}}\right)}\% \qquad (1)$$

where A_{rev} is the area under the *JV* curve for a reverse scan (from V_{OC} to J_{SC}) and A_{for} is the area under the *JV* curve for a forward scan (from J_{SC} to V_{OC}). Hysteresis measurements reveal that devices with high FAI excess have a strong tendency to show inverted hysteresis (DoH < 0), especially at low scan rates. This means that the solar cell has a lower collection of electronic carriers in the reverse scan (from V_{OC} to J_{SC}) with respect to the

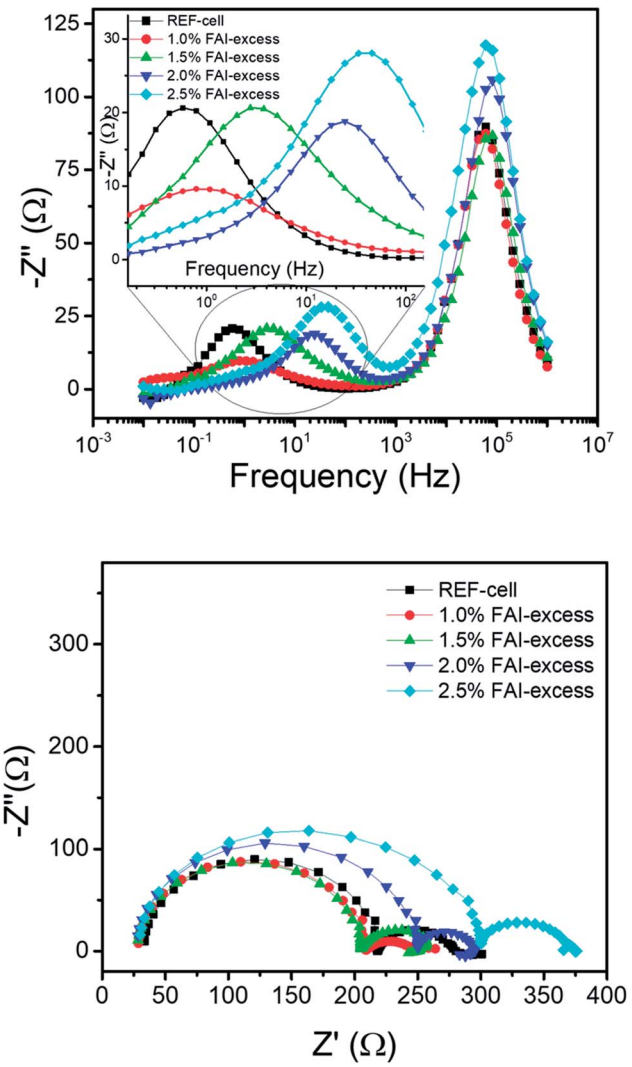

Fig. 2 Impedance response under red light illumination and at open circuit for the studied compositions. Both frequency (top) and Nyquist (bottom) plots are presented. The inset highlights the low frequency behaviour.

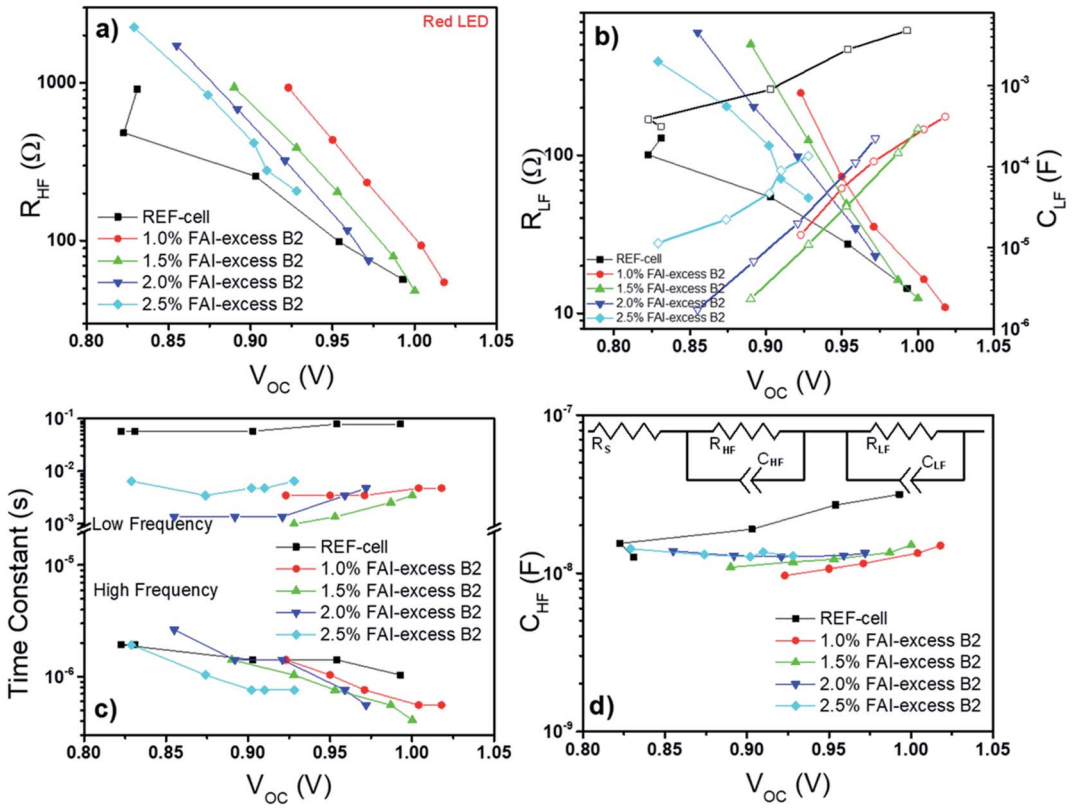

Fig. 3 Fitting results of the impedance spectra of the studied cells (batch 2): (a) high frequency resistance, (b) low frequency resistance and capacitance, (c) time constants and (d) high frequency capacitance. The equivalent circuit used is shown in panel (d).

forward scan (from J_{SC} to V_{OC}). This effect is more acute upon decreasing the scan rate.

In order to cast light on the origin of all these phenomena an impedance spectroscopy study was conducted. Impedance spectra at open circuit for all studied compositions are presented in Fig. 2, S7 and S8.†

The observed impedance response fits to the well-known pattern typically reported for PSCs with at least two arcs in the Nyquist plot, corresponding to two peaks/signals in the frequency plot, one at high frequencies (HF, 10^5 to 10^6 Hz) and other at low frequencies (LF, 0.1–10 Hz).[20,23,26,29] These spectra can conveniently be fitted to a 2RC equivalent circuit (see Fig. 3).[45] Results for the fitting parameters at open circuit, that is, low and high frequency resistances and capacitances, are presented and collected in Fig. 3.

The observed trends are again consistent with the typical behaviour in PSCs: resistances decrease exponentially with the open circuit potential, the low frequency capacitance increases exponentially (with a reciprocal slope as that of the resistance) and the high frequency capacitance varies only slightly with the open circuit potential. The latter has a very similar value for all compositions, as could be expected from its "geometrical" origin.[26] As a consequence of all these trends, the low and high frequency time constants, τ_{LF} ($=R_{LF}C_{LF}$) and τ_{HF} ($=R_{HF}C_{HF}$), have a flat and a decreasing exponential behaviour, respectively.

As discussed by Contreras *et al.*[20] and Riquelme *et al.*[26] the high frequency resistance can be related to the recombination loss of electronic carriers in the active layer. The obtained data reveal that the recombination rate gets reduced with small amounts of FAI excess (larger recombination resistance), but becomes faster with concentrations above 1.5%. This observation is in line with the variation of the V_{OC} with respect to FAI excess discussed above.

The impact of non-stoichiometry on the recombination rate is more clearly seen in Fig. 4, where the high frequency resistance is plotted *versus* open circuit voltage and composition. An optimum concentration of around 1.0–1.5% FAI excess is identified at all voltages. The impedance analysis shows that artificially creating defects in the crystalline structure initially has a beneficial effect in reducing the recombination loss and enhancing the photovoltage, but this effect becomes deleterious when the added amounts of FAI are too high. Interestingly, neither the low nor the high frequency part of the spectrum is significantly altered when the wavelength of the optical excitation is modified (see Fig. S8†). As perovskites absorb stronger in the blue, this result indicates that the spatial generation of electronic carriers within the active layer does not have a strong impact on carrier generation and that collection is very efficient in these devices (very long carrier diffusion length). A more detailed discussion of this effect supported by numerical modelling is presented in the next section.

The effect of adding an excess of FAI precursor is more evident in the low frequency part of the impedance spectrum. As observed in Fig. 2b and 3c, larger amounts of FAI excess are

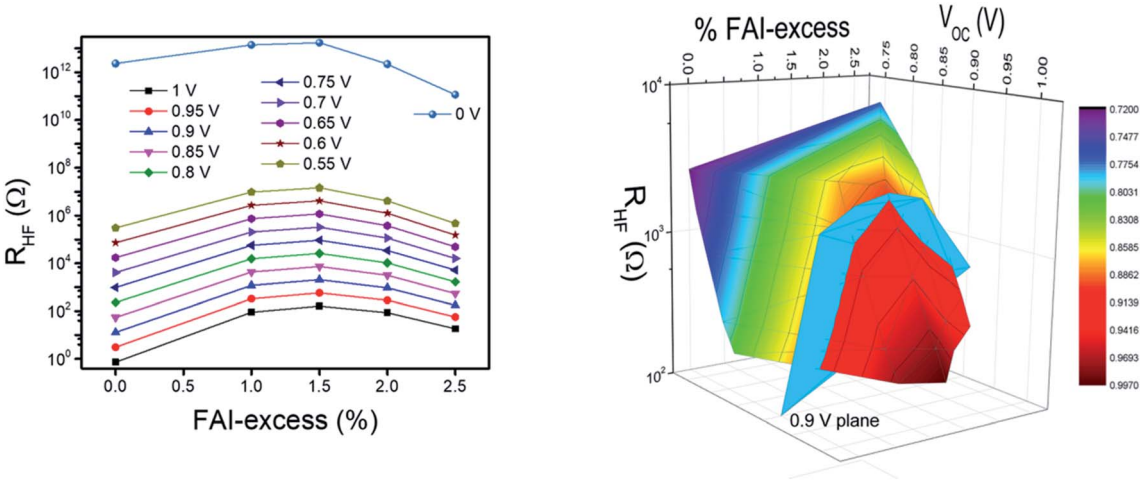

Fig. 4 High frequency resistance as a function of FAI excess and open-circuit voltage.

correlated with a consolidated shift of the low frequency signal towards higher frequency values. As discussed by several authors,[2,26,46,47] the low frequency peak of the spectrum is connected with the ion migration dynamics in the active layer of the solar cells. The ionic origin of this signal is confirmed by temperature dependent measurements (results shown in Fig. 5.)

The ion diffusion process can be quantified using Arrhenius's law, which may be adapted to extract the activation energy of the process *via*

$$\frac{1}{\tau_{LF}} = Ae^{\frac{-E_a}{k_B T}} + C \quad (2)$$

where E_a is the activation energy, k_B is Boltzmann constant, T is the absolute temperature and A, C are temperature independent constants. Results for the activation energy can be extracted from the slope of the corresponding Arrhenius plot (Fig. 5). We found that the activation energy is similar for all values of the FAI excess, of the order of 45 kJ mol^{-1} (0.45 eV). This observation suggests that the ion migration mechanism is essentially the same in all cases. However, the shift of the signal towards higher frequencies with higher values of the FAI excess indicates that the creation of crystalline defects results in an acceleration of the ionic conductivity. The ionic conductivity is a function of mobility/diffusion coefficient but also of the total concentration of ionic carriers (excess ions, vacancies).[48,49] A more detailed interpretation of these observations, supported by numerical modelling, is presented in the following section.

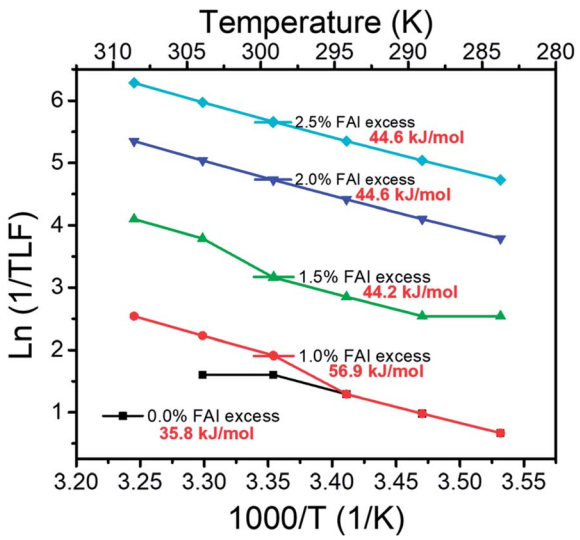

Fig. 5 Arrhenius plot of the low frequency signal in the impedance spectrum. Figures in red indicate the activation energies in kJ mol^{-1}.

4. Discussion & modelling

For the purpose of interpreting the experimental observations described in the previous section from a fundamental perspective, we have performed drift-diffusion (DD) numerical simulations to model the coupled ionic-electronic dynamics in the devices. In the DD calculations continuity equations for electrons, holes and ions (anions and cations) coupled with Poisson's equation of electrostatics are numerically solved for the stack layer: glass/ITO/PTAA/PS/C60/BCP/Cu where PS is the perovskite active layer (see Fig. 6). Energy level values and contact layers electronic properties (doping, mobilities) were taken from the literature.[42] The continuity equations include drift, diffusion, generation and recombination terms. The core of the simulation is the description of the active layer. Absorption profiles were calculated from a transfer matrix formalism using the refractive index and thickness of all the layers. Charge generation was assumed to happen directly from photon absorption but only in the active mixed perovskite[50] layer. Generation was rescaled by a factor of 1.1 to reproduce the experimental value of the short-circuit photocurrent measured under AM1.5G 1 sun illumination. This mismatch is attributed to slight differences between the actual refractive index of the samples and the literature values.[50]

Ion motion is only allowed in the perovskite layer while electron–hole transport and recombination are calculated

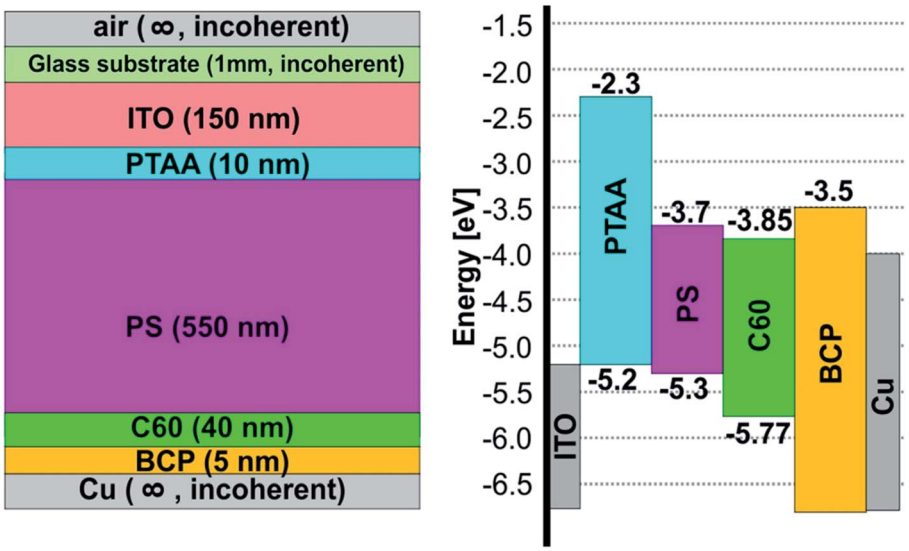

Fig. 6 Schematic of the device layout (left) and band diagram (right) used in the DD numerical simulations.

throughout all semiconductor layers. See Table 1 for the parameters used. For simplicity, we used the same mobility for both electrons and holes and a common pseudo-lifetime of 5×10^{-8} s in a trap-limited recombination mechanism in the bulk of the active layer. These values were adjusted to reproduce the experimental open-circuit voltage under AM1.5G illumination while ensuring quantitative collection at short circuit.

In order to replicate the experimental measurements, ionic parameters were varied between 10^{17} and 5×10^{18} cm^3 for the total ionic density and 6×10^{-10} and 4×10^{-9} cm^2 s^{-1} V^{-1} for the ionic mobilities.[51] In principle, only cations (attributed to iodide vacancies[1,26]) were considered mobile.

In Fig. 7 results for the steady-state simulated *JV* curves are reported. Simulations with no mobile ions reproduce quite well the photovoltaic parameters of the reference cell (no FAI excess, Fig. 1a). Addition of a relatively small amount of mobile ions results in a slight decrease of the short-circuit photocurrent and the fill factor. This effect is enhanced for larger concentrations of ionic species in the active layer. It is important to note that no change in the stationary *JV* curve is observed when the mobility of the ions is varied, instead of varying their concentration. This is not surprising as ions relax to their equilibrium ionic distributions at very long times, no matter how fast the ions move.

The simulated stationary data replicate quite well the experimental trends shown in Fig. 1a. This can be understood in the following manner: addition of an excess of precursor induces more crystalline defects creating more mobile ions (or vacancies). The presence of mobile ionic charge produces a screening effect as a consequence of the accumulation of ions at the perovskite interfaces.[26,28,52] This screening modifies the internal electric field, altering the collection of charges and hence the photocurrent. Fig. S9 in the ESI† shows the internal

Table 1 Some numerical parameters used in the DD simulations (see ESI for more details)

Electronic parameters in the active layer	
Electron mobility, μ_e	19.2 cm^2 s^{-1} V^{-1}
Hole mobility, μ_p	19.2 cm^2 s^{-1} V^{-1}
Bimolecular recombination parameter, β	9.4×10^{-10} cm^3 s^{-1}
Trap-limited electron pseudolifetime, τ_e	5×10^{-8} s
Trap-limited hole pseudolifetime, τ_p	5×10^{-8} s
Ionic parameters in the active layer	
Ion mobility (cationic)	6×10^{-10} to 4×10^{-9} cm^2 s^{-1} V^{-1}
Cationic ionic density	10^{17} to 5×10^{18} cm^3

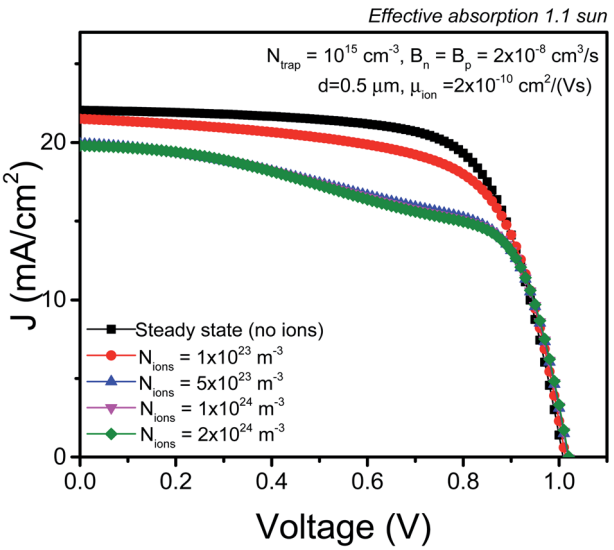

Fig. 7 Simulated *JV* curves in the steady state for different values of the concentration of ions.

electric fields at high and low values of the ion concentration. At low concentrations a negative electric field appears in the vicinity of the C60 interface for voltages close to short circuit. This field pushes holes towards the front contact and favours the collection of both holes and electrons. When the concentration of ions is increased, the screening effect is stronger and the electric field in the active layer gets effectively cancelled, not contributing to enhancing charge collection. Consequently, the short-circuit photocurrent and the fill factor become reduced with respect to the situation with no ions. From this point of view, a high concentration of mobile ions or defects is not beneficial for best performance. The detrimental effect of ions on the performance of PSCs has recently been analysed by Le Corre *et al.* with results consistent with ours.[53]

Fig. 8 and 9 show the simulated impedance spectra for different choices of the ionic parameters. The DD numerical results indicate that both a change in the ionic mobility and a change in the ion density can explain the shift of the low frequency peak observed in the experiments without altering the high frequency peak (Fig. 2b). In previous work by some of the authors[26] and others[23,31] it was found that the ionic properties are mostly revealed in the low frequency part of the spectrum. This is clearly observed in the simulated spectra. However, a distinctive feature makes the effect produced by the mobility and the ion density different. Only a change in the latter modifies the low frequency arc, as observed in the experiments (Fig. 2a). This observation points to an increase of the ion density provoked by the creation of crystalline defects as the main reason for the observed experimental behaviour. A constant value of the ion mobility of 6×10^{-10} cm^2 s^{-1} V^{-1} ($D_{ion} \approx 10^{-11}$ cm^2 s^{-1}) seems to reproduce well the low frequency peaks detected in the experiments, in line with the predictions for the ion diffusion coefficient from atomistic simulations recently reported.[51] Furthermore, both the ion mobility and the ion concentration inferred from the DD analysis of the experimental data coincide quite well with the values reported by Futscher and coworkers using temperature-dependence capacitance measurements.[34,35] A poorer agreement is found when comparing with the data deduced by Fischer *et al.* using a combination of time domain measurements and DD modelling.[36]

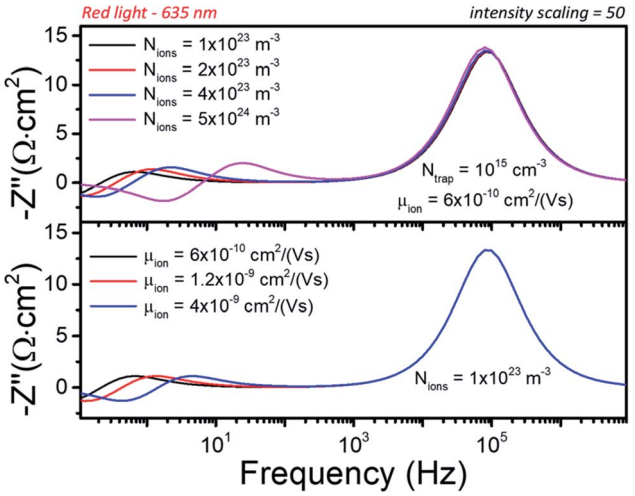

Fig. 8 Simulated frequency impedance plots for different values of the concentration of ions (top) and the ion mobility (bottom).

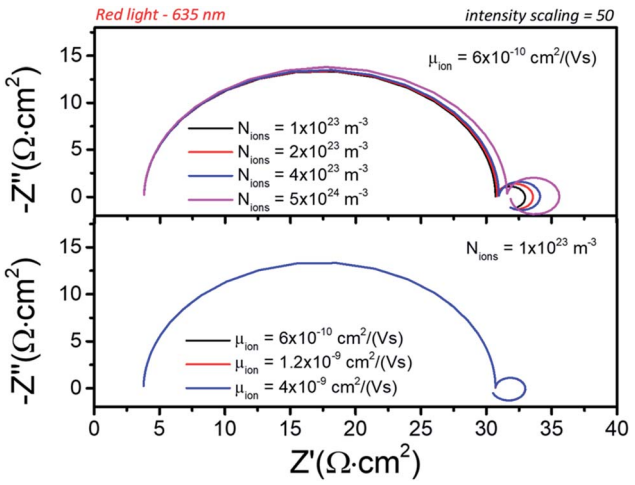

Fig. 9 Simulated Nyquist impedance plots for different values of the concentration of ions (top) and the ion mobility (bottom).

A constant ion mobility and varying ion concentration is a scenario that also explains the results obtained for *JV* curves (Fig. 1a) and the activation energy for ion migration (Fig. 5). Regarding the former, the simulated stationary *JV* curves only change when the ion concentration is varied, not the mobility, confirming this interpretation. On the other hand, the activation energy for ion migration does not change significantly with the FAI excess. The increment in the concentration of mobile ionic charge shifts the spectrum towards higher frequencies, but the migration mechanism of individual ions remains the same, hence the nearly constant activation energy.

It is interesting to check if the DD modelling can also reproduce the observed hysteresis behaviour. Fig. S10 in the ESI† shows simulated transient *JV* curves for several choices of the ionic parameters. The bottom line of this study is that a low value of the ionic density leads to regular hysteresis (DoH > 0 in eqn (1)), whereas a high concentration of mobile ions (or absence of them) remove all hysteretic effects. This is explained by the change of slope in the internal electric field in the reverse scan (which favours electron collection) with respect to the forward scan (which hampers collection).[24,26] This effect is clearly reproduced by the DD simulations (see Fig. S11†) at low ion concentrations.

Unfortunately, the appearance of inverted hysteresis at low scan rates is not observed for any combination of model parameters, pointing to a different mechanism associated to the relatively high concentration of mobile ionic charge and crystalline defects. In this respect, Jacobs *et al.*[54] suggested that the hysteresis may become inverted depending on the relative values of the scan rate and the position of the low frequency peak. Passivation of the interfaces can affect significantly the degree of hysteresis due to the reduction of the recombination loss and the lengthening of the diffusion length, as shown by

Neukom *et al.*[27] Alvarez and coworkers.[55] made a connection between inverted hysteresis and negative capacitance features. In any case, this phenomenon is complex because the simple DD model used here, in spite of its good overall performance to explain the *JV* curves and the impedance spectra, is not capable to reproduce the crossover to inverted hysteresis at low scan rates. Consequently, further investigation about its origins is required.

As noted in the previous section, the addition of FAI excess and the subsequent departure from the stoichiometric composition also has an impact on the open circuit voltage of the solar cell. This points to a change in the recombination rate and/or the recombination mechanism. In recent work it has been shown that ionic features can also affect the recombination parameters and complicate the interpretation of the impedance spectrum and the ideality factor.[22,26,30,56] Recently, Bennett and coworkers[30] have proposed an "electronic" ideality factor which is not "contaminated" by the ionic properties of the sample. This quantity is calculated *via*

$$n_{el} = \frac{qR_{hf}\, J_{rec}(V_{DC})}{k_B T} \quad (3)$$

where q is the elementary charge, R_{hf} is the high frequency resistance described before and J_{rec} the DC recombination current. The two latter quantities can be extracted from the impedance spectra at open circuit described in the previous section. The electronic ideality factor is a true analogue of the classical ideality factor, which is valid for the coupled electronic-ionic physics of perovskite solar cells. As such, it can be used to appropriately determine the dominant recombination mechanism, in the same way the ideality factor is used in classical theory. Thus, an electronic ideality factor close to 1 is an indicative of dominant surface recombination (ruling out bimolecular recombination) whereas a value close to 2 points to bulk trap-limited recombination.[19,30]

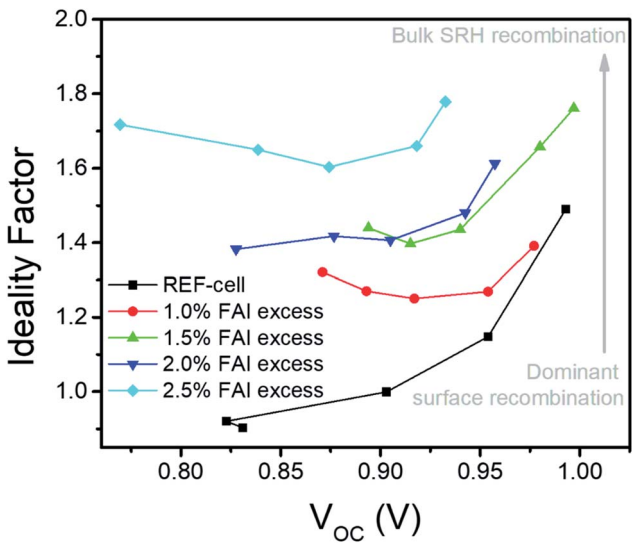

Fig. 10 Electronic ideality factors calculated with eqn (3) for the samples studied.

In Fig. 10 the electronic ideality factors obtained after application of eqn (3) to the impedance data is presented. The ideality factors are presented as a function of the open circuit voltage. Regardless of the experimental uncertainty, the results evidence a consistent shift of values close to 1, to values close to 2 with increasing FAI excess. According to theory, this would mean that the creation of crystalline effects as a consequence of the breaking of the stoichiometry leads to enhancement of the bulk recombination rate with respect to surface recombination. However, this effect does not rule out a reduction of the surface recombination contribution upon addition of FAI, as also observed by Boyd *et al.*[39] The interplay between these two mechanisms: (1) decrease of the overall recombination rate due to minimization of surface recombination routes and (2) enhancement of defect-assisted bulk recombination, can explain the existence of an "optimum" in the amount of FAI excess added. For that optimum the overall recombination rate reaches a minimum and the V_{OC} and recombination resistance are maximized.

Following Bennet and coworkers (ref. 30) it is possible to estimate the relative contributions of surface and bulk recombination *via* the expression

$$n_{el} = \frac{2}{2 - r} \quad (4)$$

where r is the ratio of the bulk trap-mediated recombination current to the total recombination current. Using this expression and the data of Fig. 10, one can estimate $r \approx 1$ for the stoichiometric cell and $r \approx 0.88$ for the device with 2.5% FAI excess.

Finally, it is worthwhile to analyse the impact of the higher amount of mobile ionic charge on the short-term stability of the devices. Contrary to what one would expect, a large concentration of mobile ions, as evidenced by the impedance results and the modelling predictions, leads to better stability under light soaking conditions (Fig. 1b). This observation suggests the occurrence of a sort of "curing" effect associated to the presence of mobile crystalline defects. For instance, deQuilettes *et al.*[57] reported a "curing" effect (reduction of the electronic trap density) due to halide migration upon illumination. A similar effect can explain the stable photocurrent under light soaking for the non-stoichiometric samples (Fig. 1, S2 and S3†) when the illumination is increased (Fig. 10). This mechanism would imply that a larger "fluidity" of the perovskite is beneficial for more stable devices, at least in the short-term. The larger availability of mobile ionic defects can also be behind the larger inverted hysteresis at low scan rates.

5. Conclusions

The implications of using non-stoichiometric compositions in mixed perovskite solar cells has been studied by a combination of experiments and drift-diffusion simulations. For caesium/formamidinium inverted solar cells devices, it is observed that using a slight excess of formamidinium precursor in the perovskite composition deteriorates the short-circuit photocurrent and the fill factor, but also leads to more stable devices

under light soaking. The open-circuit voltage exhibits a non-monotonic behaviour with respect to the amount of precursor added, leading to an optimum concentration of around 1–1.5% excess. Impedance spectroscopy studies at open-circuit and analysis of the electronic ideality factor show that this is a consequence of a change in the recombination mechanism (from dominant surface recombination to more bulk recombination) when the stoichiometry is broken. The impedance spectroscopy results also show an acceleration of the low frequency dynamics in the solar cell. Drift-diffusion simulations indicate that the shift of the low frequency signals and the change in the photovoltaic parameters are consistent with an increase of the concentration of ionic mobile charge when a larger amount of excess formamidinium is present in the sample. We attribute this effect to the creation of crystalline defects when the sample is non-stoichiometric and excess ions turn "mobile".

Conflicts of interest

There are no conflicts to declare.

Acknowledgements

This work was funded by the Ministerio de Ciencia e Innovación of Spain, Agencia Estatal de Investigación (AEI) and EU (FEDER) under grants PID2019-110430GB-C22 and PCI2019-111839-2 (SCALEUP) and Junta de Andalucia under grant SOLARFORCE (UPO-1259175). The work was also funded by FORDECYT-PRONACES projects 318703 and 848260, and the Royal Society under grant number ICA-R1-191321. The authors gratefully acknowledge support from the Ministerio de Universidades and Universidad Pablo de Olavide through the Beatriz Galindo program under project BEAGAL 18/00077 and grant BGP 18/00060. AJR thanks the Spanish Ministerio de Educación, Cultura y Deporte for its supports *via* a PhD grant (FPU2017-03684). LJB is supported by an EPSRC funded studentship from the CDT in New and Sustainable Photovoltaics, reference EP/L01551X/1. RE acknowledges postdoctoral support from Conacyt, under grant numbers 770670 and 801029. We thank Dr Courtier for her extremely useful comments and discussions about this work.

References

1 C. Eames, J. M. Frost, P. R. F. Barnes, B. C. O'Regan, A. Walsh and M. S. Islam, *Nat. Commun.*, 2015, **6**, 7497.
2 J.-P. Correa-Baena, M. Anaya, G. Lozano, W. Tress, K. Domanski, M. Saliba, T. Matsui, T. J. Jacobsson, M. E. Calvo, A. Abate, M. Grätzel, H. Míguez and A. Hagfeldt, *Adv. Mater.*, 2016, **28**, 5031–5037.
3 *Best Research-Cell Efficiency Chart*, **https://www.nrel.gov/pv/cell-efficiency.html**, accessed 29 December 2021.
4 S. N. Habisreutinger, N. K. Noel and H. J. Snaith, *ACS Energy Lett.*, 2018, **3**, 2472–2476.
5 P. Fassl, V. Lami, A. Bausch, Z. Wang, M. T. Klug, H. J. Snaith and Y. Vaynzof, *Energy Environ. Sci.*, 2018, **11**, 3380–3391.
6 N. H. Tiep, Z. Ku and H. J. Fan, *Adv. Energy Mater.*, 2016, **6**, 1501420.
7 J. A. Christians, S. N. Habisreutinger, J. J. Berry and J. M. Luther, *ACS Energy Lett.*, 2018, **3**, 2136–2143.
8 L. Meng, J. You and Y. Yang, *Nat. Commun.*, 2018, **9**, 5265.
9 Y. Yuan and J. Huang, *Acc. Chem. Res.*, 2016, **49**, 286–293.
10 E. T. Hoke, D. J. Slotcavage, E. R. Dohner, A. R. Bowring, H. I. Karunadasa and M. D. McGehee, *Chem. Sci.*, 2015, **6**, 613–617.
11 M. C. Brennan, S. Draguta, P. V. Kamat and M. Kuno, *ACS Energy Lett.*, 2018, **3**, 204–213.
12 M. Saliba, T. Matsui, J.-Y. Seo, K. Domanski, J.-P. Correa-Baena, M. K. Nazeeruddin, S. M. Zakeeruddin, W. Tress, A. Abate, A. Hagfeldt and M. Grätzel, *Energy Environ. Sci.*, 2016, **9**, 1989–1997.
13 H. Min, M. Kim, S.-U. Lee, H. Kim, G. Kim, K. Choi, J. H. Lee and S. I. Seok, *Science*, 2019, **366**, 749–753.
14 H. Min, D. Y. Lee, J. Kim, G. Kim, K. S. Lee, J. Kim, M. J. Paik, Y. K. Kim, K. S. Kim, M. G. Kim, T. J. Shin and S. Il Seok, *Nature*, 2021, **598**, 444–450.
15 T. M. Koh, K. Fu, Y. Fang, S. Chen, T. C. Sum, N. Mathews, S. G. Mhaisalkar, P. P. Boix and T. Baikie, *J. Phys. Chem. C*, 2014, **118**, 16458–16462.
16 D. P. McMeekin, G. Sadoughi, W. Rehman, G. E. Eperon, M. Saliba, M. T. Hörantner, A. Haghighirad, N. Sakai, L. Korte, B. Rech, M. B. Johnston, L. M. Herz and H. J. Snaith, *Science*, 2016, **351**, 151–155.
17 S. Masi, C. Echeverría-Arrondo, K. M. M. Salim, T. T. Ngo, P. F. Mendez, E. López-Fraguas, D. F. Macias-Pinilla, J. Planelles, J. I. Climente and I. Mora-Seró, *ACS Energy Lett.*, 2020, **5**, 418–427.
18 K. M. M. Salim, S. Masi, A. F. Gualdrón-Reyes, R. S. Sánchez, E. M. Barea, M. Krečmarová, J. F. Sánchez-Royo and I. Mora-Seró, *ACS Energy Lett.*, 2021, **6**, 3511–3521.
19 W. Tress, M. Yavari, K. Domanski, P. Yadav, B. Niesen, J. P. C. Baena, A. Hagfeldt and M. Graetzel, *Energy Environ. Sci.*, 2018, **11**, 151–165.
20 L. Contreras-Bernal, S. Ramos-Terrón, A. Riquelme, P. P. Boix, J. Idígoras, I. Mora-Seró and J. A. Anta, *J. Mater. Chem. A*, 2019, **7**, 12191–12200.
21 M. Stolterfoht, C. M. Wolff, J. A. Márquez, S. Zhang, C. J. Hages, D. Rothhardt, S. Albrecht, P. L. Burn, P. Meredith, T. Unold and D. Neher, *Nat. Energy*, 2018, **3**, 847.
22 A. Castro-Chong, A. J. Riquelme, T. Aernouts, L. J. Bennett, G. Richardson, G. Oskam and J. A. Anta, *ChemPlusChem*, 2021, **86**, 1347–1356.
23 A. Pockett, G. E. Eperon, N. Sakai, H. J. Snaith, L. M. Peter and P. J. Cameron, *Phys. Chem. Chem. Phys.*, 2017, **19**, 5959–5970.
24 N. E. Courtier, J. M. Cave, J. M. Foster, A. B. Walker and G. Richardson, *Energy Environ. Sci.*, 2018, **12**, 396–409.
25 S. Ravishankar, O. Almora, C. Echeverría-Arrondo, E. Ghahremanirad, C. Aranda, A. Guerrero, F. Fabregat-Santiago, A. Zaban, G. Garcia-Belmonte and J. Bisquert, *J. Phys. Chem. Lett.*, 2017, **8**, 915–921.

26 A. Riquelme, L. J. Bennett, N. E. Courtier, M. J. Wolf, L. Contreras-Bernal, A. B. Walker, G. Richardson and J. A. Anta, *Nanoscale*, 2020, **12**, 17385–17398.
27 M. T. Neukom, S. Züfle, E. Knapp, M. Makha, R. Hany and B. Ruhstaller, *Sol. Energy Mater. Sol. Cells*, 2017, **169**, 159–166.
28 G. Richardson, S. E. J. O'Kane, R. G. Niemann, T. A. Peltola, J. M. Foster, P. J. Cameron and A. B. Walker, *Energy Environ. Sci.*, 2016, **9**, 1476–1485.
29 I. Zarazua, G. Han, P. P. Boix, S. Mhaisalkar, F. Fabregat-Santiago, I. Mora-Seró, J. Bisquert and G. Garcia-Belmonte, *J. Phys. Chem. Lett.*, 2016, **7**, 5105–5113.
30 L. J. Bennett, A. J. Riquelme, N. E. Courtier, J. A. Anta and G. Richardson, ArXiv210511226 Cond-Mat Physicsphysics.
31 R. García-Rodríguez, D. Ferdani, S. Pering, P. J. Baker and P. J. Cameron, *J. Mater. Chem. A*, 2019, **7**, 22604–22614.
32 W. Peng, C. Aranda, O. M. Bakr, G. Garcia-Belmonte, J. Bisquert and A. Guerrero, *ACS Energy Lett.*, 2018, 1477–1481.
33 A. Riquelme, F. E. Gálvez, L. Contreras-Bernal, H. Míguez and J. A. Anta, *J. Appl. Phys.*, 2020, **128**, 133103.
34 M. H. Futscher, J. M. Lee, L. McGovern, L. A. Muscarella, T. Wang, M. I. Haider, A. Fakharuddin, L. Schmidt-Mende and B. Ehrler, *Mater. Horiz.*, 2019, **6**, 1497–1503.
35 M. H. Futscher, M. K. Gangishetty, D. N. Congreve and B. Ehrler, *J. Chem. Phys.*, 2020, **152**, 044202.
36 M. Fischer, D. Kiermasch, L. Gil-Escrig, H. J. Bolink, V. Dyakonov and K. Tvingstedt, *Sustainable Energy Fuels*, 2021, **5**, 3578–3587.
37 C. Li, A. Guerrero, Y. Zhong, A. Gräser, C. A. M. Luna, J. Köhler, J. Bisquert, R. Hildner and S. Huettner, *Small*, 2017, **13**, 1701711.
38 W. Song, X. Zhang, S. Lammar, W. Qiu, Y. Kuang, B. Ruttens, J. D'Haen, I. Vaesen, T. Conard, Y. Abdulraheem, T. Aernouts, Y. Zhan and J. Poortmans, *ACS Appl. Mater. Interfaces*, 2022, **14**, 27922–27931.
39 C. C. Boyd, R. C. Shallcross, T. Moot, R. Kerner, L. Bertoluzzi, A. Onno, S. Kavadiya, C. Chosy, E. J. Wolf, J. Werner, J. A. Raiford, C. de Paula, A. F. Palmstrom, Z. J. Yu, J. J. Berry, S. F. Bent, Z. C. Holman, J. M. Luther, E. L. Ratcliff, N. R. Armstrong and M. D. McGehee, *Joule*, 2020, **4**, 1759–1775.
40 Y. Deng, S. Xu, S. Chen, X. Xiao, J. Zhao and J. Huang, *Nat. Energy*, 2021, **6**, 633–641.
41 L. Rakocevic, F. Ernst, N. T. Yimga, S. Vashishtha, T. Aernouts, T. Heumueller, C. J. Brabec, R. Gehlhaar and J. Poortmans, *Sol. RRL*, 2019, **3**, 1800287.
42 M. T. Neukom, A. Schiller, S. Züfle, E. Knapp, J. Ávila, D. Pérez-del-Rey, C. Dreessen, K. P. S. Zanoni, M. Sessolo, H. J. Bolink and B. Ruhstaller, *ACS Appl. Mater. Interfaces*, 2019, **11**, 23320–23328.
43 S. J. Yoon, M. Kuno and P. V. Kamat, *ACS Energy Lett.*, 2017, **2**, 1507–1514.
44 S. J. Yoon, S. Draguta, J. S. Manser, O. Sharia, W. F. Schneider, M. Kuno and P. V. Kamat, *ACS Energy Lett.*, 2016, **1**, 290–296.
45 A. Todinova, L. Contreras-Bernal, M. Salado, S. Ahmad, N. Morillo, J. Idígoras and J. A. Anta, *ChemElectroChem*, 2017, **4**(11), 2891–2901.
46 D. Moia, I. Gelmetti, P. Calado, W. Fisher, M. Stringer, O. Game, Y. Hu, P. Docampo, D. Lidzey, E. Palomares, J. Nelson and P. R. F. Barnes, *Energy Environ. Sci.*, 2019, **12**, 1296–1308.
47 L. Contreras, J. Idígoras, A. Todinova, M. Salado, S. Kazim, S. Ahmad and J. A. Anta, *Phys. Chem. Chem. Phys.*, 2016, **18**, 31033–31042.
48 D. Barboni and R. A. D. Souza, *Energy Environ. Sci.*, 2018, **11**, 3266–3274.
49 S. R.-G. Balestra, J. M. Vicent-Luna, S. Calero, S. Tao and J. A. Anta, *J. Mater. Chem. A*, 2020, **8**, 11824–11836.
50 J. Werner, G. Nogay, F. Sahli, T. C.-J. Yang, M. Bräuninger, G. Christmann, A. Walter, B. A. Kamino, P. Fiala, P. Löper, S. Nicolay, Q. Jeangros, B. Niesen and C. Ballif, *ACS Energy Lett.*, 2018, **3**, 742–747.
51 J. A. Seijas-Bellido, B. Samanta, K. Valadez-Villalobos, J. J. Gallardo, J. Navas, S. R. G. Balestra, R. M. Madero Castro, J. M. Vicent-Luna, S. Tao, M. C. Toroker and J. A. Anta, *J. Chem. Inf. Model.*, 2022, DOI: **10.1021/acs.jcim.1c01506**.
52 O. Almora, I. Zarazua, E. Mas-Marza, I. Mora-Sero, J. Bisquert and G. Garcia-Belmonte, *J. Phys. Chem. Lett.*, 2015, **6**, 1645–1652.
53 V. M. Le Corre, J. Diekmann, F. Peña-Camargo, J. Thiesbrummel, N. Tokmoldin, E. Gutierrez-Partida, K. P. Peters, L. Perdigón-Toro, M. H. Futscher, F. Lang, J. Warby, H. J. Snaith, D. Neher and M. Stolterfoht, *Sol. RRL*, 2022, **6**, 2100772.
54 D. A. Jacobs, H. Shen, F. Pfeffer, J. Peng, T. P. White, F. J. Beck and K. R. Catchpole, *J. Appl. Phys.*, 2018, **124**, 225702.
55 A. O. Alvarez, R. Arcas, C. A. Aranda, L. Bethencourt, E. Mas-Marzá, M. Saliba and F. Fabregat-Santiago, *J. Phys. Chem. Lett.*, 2020, 8417–8423.
56 N. E. Courtier, *Phys. Rev. Appl.*, 2020, **14**, 024031.
57 D. W. deQuilettes, W. Zhang, V. M. Burlakov, D. J. Graham, T. Leijtens, A. Osherov, V. Bulović, H. J. Snaith, D. S. Ginger and S. D. Stranks, *Nat. Commun.*, 2016, **7**, 11683.

